1 **Sensitivity of Arctic clouds to ice microphysical processes in the NorESM2 climate**

2 **model**

3

4 Georgia Sotiropoulou[1,3*], Anna Lewinschal[2], Paraskevi Georgakaki[3], Vaughan Phillips[4],

5 Sachin Patade[4], Annica M. L. Ekman[2], Athanasios Nenes[1,3]

6

7 [1]ICE-HT, Foundation for Research and Technology Hellas (FORTH), Patras, Greece

8 [2]Department of Meteorology, Stockholm University & Bolin Center for Climate Research,

9 Sweden

10 [3]Laboratory of Atmospheric Processes and their Impacts (LAPI), Ecole Polytechnique

11  Fédérale de Lausanne (EPFL), Lausanne, Switzerland

12 [4]Department of Physical Geography, University of Lund, Lund, Sweden

13

14 *Currently at the Department of Physics, Sector of Environmental Physics & Meteorology,*

15 *National & Kapodistrian University of Athens, Greece*

16

17 Corresponding author: georgia.sotiropoulou@epfl.ch , athanasios.nenes@epfl.ch

18

21

22

23 **Abstract**

24 Ice formation remains one of the most poorly represented microphysical processes in climate

25 models. While primary ice production (PIP) parameterizations are known to have a large

26 influence on the modeled cloud properties, the representation of secondary ice production

27 (SIP) is incomplete and its corresponding impact is therefore largely unquantified.

28 Furthermore, ice aggregation is another important process for the total cloud ice budget,

29 which also remains largely unconstrained. In this study we examine the impact of PIP, SIP

30 and ice aggregation on Arctic clouds, using the Norwegian Earth System model version 2

31 (NorESM2). Simulations with both prognostic and diagnostic PIP show that heterogeneous

32 freezing alone cannot reproduce the observed cloud ice content. The implementation of

33 missing SIP mechanisms (collisional break-up, drop-shattering and sublimation break-up) in

34   NorESM2 improves the modeled ice properties, while improvements in liquid content occur

35   only in simulations with prognostic PIP. However, results are sensitive to the description of

36   collisional break-up. This mechanism, which dominates SIP in the examined conditions, is

37   very sensitive to the treatment of the sublimation correction factor, a poorly-constrained

38   parameter that is included in the utilized parameterization. Finally, variations in ice

39   aggregation treatment can also significantly impact cloud properties, mainly through its

40   impact on collisional break-up efficiency. Overall, enhancement in ice production though the

41   addition of SIP mechanisms and the reduction of ice aggregation (in line with radar

42   observations of shallow Arctic clouds) result in enhanced cloud cover and decreased TOA

43   radiation biases, compared to satellite measurements, especially during the cold months.

44

45   **Significance**

46   Arctic clouds remain a large source of uncertainty in projections of the future climate due to

47   the poor representation of the microphysical processes that govern their life cycle. Ice

48   formation is among the least understood processes. While it is widely recognized that better

49   constraints on primary ice production (PIP) are needed to improve existing parameterizations,

50   we show that secondary ice production (SIP) and ice aggregation can have also a significant

51   impact on the ice number concentrations. Constraining ice formation through the addition of

52   missing SIP mechanisms and reducing ice aggregation can improve the representation of the

53   cloud macrophysical properties and enhance total cloud cover in the Arctic region, which in

54   turn contributes to decreased TOA radiation biases in the cold months.

55

56   **1. Introduction**

57   Clouds and cloud feedbacks remain the largest source of uncertainty in predictions of the

58   future climate (Boucher et al. 2013). In the most recent Climate Model Intercomparison

59   Project (phase 6 – CMIP6) many general circulation models (GCMs) exhibited larger

60   sensitivity to changes in carbon dioxide concentrations, a metric known as Equilibrium

61   Climate Sensitivity (ECS), compared to CMIP5 models (Zelinka et al. 2020). Murray et al.

62   (2021) showed that ECS values in CMIP6 correlate with mid-to-high latitude low-level cloud

63   feedbacks. Moreover, CMIP6 models suffer from biases in high-latitude cloud cover (Vignesh

64   et al. 2020), cloud radiative impacts (Sledd and L'ecuyer 2020) and snowfall patterns

65   (Thomas et al. 2019).

66        Mixed-phase clouds, consisting of both supercooled liquid and ice, are the most

2

67    abundant Arctic cloud type at temperatures between -25$^{o}$C and 0$^{o}$C (Shupe et al. 2006; 2011).

68    While these clouds are theoretically thermodynamically unstable and can easily glaciate

69    through the Wegener-Bergeron-Findeisen (WBF) mechanism, they have been observed to

70    persist for days to weeks (Morrison et al. 2012). Moreover, as ice crystals grow through vapor

71    deposition, they can start forming aggregates through collisions with other ice particles or

72    they can gain mass through the collection of liquid droplets (i.e. riming) until they eventually

73    fall out in the form of snow or graupel. Mixed-phase cloud observations often indicate that the

74    supercooled liquid layer is concentrated near cloud top with ice particles falling below, which

75    allows the liquid phase to be maintained (Morrison et al. 2012). Modeling the life-cycle of

76    these clouds is challenging since errors in the representation of the complex processes that

77    maintain them can lead to rapid glaciation. At the same time a correct representation of the

78    vertical structure and cloud phase is crucial for an accurate estimation of the cloud radiative

79    impact (Curry et al. 1996). Predictions of Arctic warming are particularly sensitive to cloud

80    ice formation (Tan et al. 2019). While ice formation processes are likely an important

81    contributor to the CMIP6 spread in predicted mid- and high-latitude cloud feedbacks (Murray

82    et al. 2021), they remain among the most poorly understood microphysical processes in

83    mixed-phase clouds (Seinfeld et al. 2016; Storelvmo 2017).

84    Primary ice production (PIP) at temperatures above -38$^{o}$C can only happen

85    heterogeneously in the atmosphere, which means that the assistance of insoluble aerosols that

86    act as Ice Nucleating Particles (INPs) is required (Hoose and Möhler 2012). However,

87    primary ice crystal concentrations can further be enhanced through multiplication processes

88    (Field et al. 2017; Korolev and Leisner 2020), known as secondary ice production (SIP). SIP

89    has received substantially less attention than PIP in the past decades, which is the reason

90    behind its poor (or absent) representation in atmospheric models. Several observational

91    (Gayet et al. 2009; Lloyd et al. 2015; Luke et al. 2021; Pasquier et al. 2022) and modeling

92    (Sotiropoulou et al. 2020; 2021b; Zhao et al. 2021; Zhao and Liu 2021; 2022) studies have

93    indicated that SIP might be particularly important for Arctic clouds, as INP concentrations in

94    the Arctic region are generally low (Wex et al. 2020) to account for the high ice crystal

95    number concentrations (ICNCs) observed (Hobbs and Rangno 1998).

96    Several mechanisms that can trigger ice multiplication have been identified in

97    laboratory experiments (Korolev and Leisner 2020), however only one SIP mechanism has

98    until now been considered in GCMs: the Hallett-Mossop (HM) process (Hallett and Mossop,

99    1974). This is also the case for the Norwegian Earth System model version 2 (NorESM2),

which allows HM to occur after cloud drop-snow collisions. However, observational (Rangno and Hobbs 2001; Schwarzenboeck et al. 2009; Luke et al. 2021) and modeling studies (Sotiropoulou et al. 2020; 2021b; Zhao et al. 2021; Zhao and Liu 2021; 2022) suggest that other SIP processes, like collisional break-up (Vardiman 1978; Takahashi et al. 1995) and drop-shattering (Lauber et al. 2018; Keinert et al. 2020), also have a significant influence on Arctic cloud microphysical structure.

In this study we implement descriptions for drop-shattering (DSH) and collisional break-up (BR) in NorESM2, using parameterizations from the recent literature (Phillips et al. 2017a,b; 2018). We further test the efficiency of sublimation break-up (SUBBR) (Oraltay and Hallett 1989; Bacon et al. 1998), a process whose efficiency remains unknown in Arctic atmospheric conditions, using the parameterization developed by Deshmukh et al. (2022). In addition, we modify the existing HM description to further account for rain-snow collisions. Sensitivity simulations with varying PIP, SIP and ice aggregation treatment are conducted to quantify the ice-related processes that are most impactful on ice particle number. Results are initially evaluated against two-year surface-based observations from Ny-Ålesund for the period June 2016 - May 2018 to assess the most realistic simulation set-up. Satellite radiation and cloud measurements are further used to quantify the impact of the examined processes on the current climate state over the whole Arctic region.

**2. Methods**

*a. Observations*

Field observations of clouds were collected at Ny-Ålesund in 2016–2018 in the context of the Arctic Amplification: Climate Relevant Atmospheric and Surface Processes, and Feedback Mechanisms (AC)[3] project. With the addition of a W-band cloud radar, this observation site became one of the few Arctic sites capable of state-of-the-art long-term cloud profiling with high temporal and spatial resolution. A detailed analysis of the observed cloud properties is offered by Nomokonova et al. (2019; 2020). The total occurrence of clouds was found to be ~81%. The most predominant type of clouds was multi-layer clouds with a frequency of occurrence of 44.8%. Single-layer clouds occurred 36%, with the vast majority of them being mixed-phase; liquid hydrometeors were generally observed within the lowest two kilometers in the atmosphere.

132   Below the measurements utilized to evaluate the model are described. Macro- and

133 micro- physical cloud properties are derived from a combination of instruments that includes

134 a 94 GHz cloud radar, a ceilometer and a HATPRO radiometer (Nomokonova et al. 2019d).

135 The cloud Liquid water path (LWP) is derived from a HATPRO microwave radiometer

136 (Nomokonova et al. 2019a,b,c) with typical uncertainty around +/- 20–25 g m$^{-2}$, using a

137 multivariate linear regression algorithm developed at the University of Cologne (Löhnert and

138 Crewell 2003). HATPRO cannot provide reliable estimates under rainy conditions, when the

139 instrument radome becomes wet; data flagged for precipitation are excluded from this

140 analysis. Thermodynamic variables such as temperature (Nomokovova et al. 2019d,e,f) and

141 integrated water vapor (IWV; Nomokovova et al. 2019g,h,i) are also derived from HATPRO.

142   Once the Cloudnet retrieval algorithm (Illingworth et al. 2007) has been applied to

143 categorize the measured particles as liquid droplets, ice, melting ice, and drizzle/rain, ice

144 water content (IWC) is derived from radar reflectivity and temperature measurements

145 following the methodology of Hogan et al. (2006). The uncertainties in this IWC retrieval

146 range from -33% to +50% for temperatures above -20$^{o}$C and from -50% to +100% for

147 temperatures below -40$^{o}$C. The effective radius of ice particles ($r_{ieff}$) is calculated

148 following Delanoë and Hogan (2010), using IWC and visible extinction coefficient estimates

149 (Ebell et al. 2020); the latter is also derived following Hogan et al. (2006). The uncertainty in

150 $r_{ieff}$ retrieval described by Delanoë and Hogan (2010) is about 30%, while the uncertainty for

151 the radar-derived visible extinction coefficient that is used in the ice effective radii retrieval is

152 62% to 160% (Hogan et al. 2006). de Boer et al. (2009) reported that assumptions in the shape

153 of ice particles might result in a 200 μm uncertainty in $r_{ieff}$ estimations that are based on cloud

154 radar and lidar techniques.

155   Surface in-situ cloud measurements were collected at the Zeppelin station, on mount

156 Zeppelin near Ny-Alesund town, with the Zeppelin Observatory counterflow virtual impactor

157 (CVI) inlet and a fog monitor (Droplet Measurement Technologies Inc., USA, Model FM-

158 120) (Karlsson et al. 2021a,b) for a similar period (until February 2018) as the remote sensing

159 observations. CVI and FM-120 number concentrations show very good agreement, except for

160 a small portion of the data (7-8%) that are characterized by overestimated CVI values

161 (Karlsson et al. 2021a). These deviations have been attributed to either varying sampling

162 efficiencies, physical processes or spurious measurements (Karlsson et al. 2021a). FM-120 is

163 used in our study to evaluate the modeled cloud particle spectrum over a limited size range,

164 since these instruments measure only small cloud particles with diameters below 50 μm.

165       Finally, since Ny-Alesund conditions differ from those observed at other pan-Arctic

166    sites and in the central Arctic, in terms of both thermodynamic (e.g. Naaka et al. 2018) and

167    aerosol (e.g. Schmeisser et al. 2018) properties, this is expected to lead in a variable impact of

168    the examined processes across the Arctic. For this reason, local measurements are

169    complemented with satellite datasets to evaluate the modeled radiation and cloud

170    characteristics over the whole Arctic region. These include the Clouds and Earth's Radiant

171    Energy Systems (CERES; Wielicki et al. 1996) Energy Balanced and Filled (EBAF) product,

172    edition 4.1 (Kato et al. 2018) and the GCM-Oriented CALIPSO Cloud Product (GOCCP)

173    Version 3 (Chepfer et al. 2010).

### b. Model description

175    For our investigations we use the NorESM2-MM version (Selund et al. 2021) with

176    approximately $1^{o}$ horizontal resolution (development branch). Wind and pressure fields are

177    nudged towards ERA-Interim profiles to limit the influence of meteorological errors on

178    microphysical fields. The relaxation time for nudging is set to 6 hours, same as the time

179    resolution of the reanalysis data (Dee et al. 2011). Simulations are run for 29 months, from 1

180    January 2016 to 31 May 2018, with fixed sea-surface temperatures (SSTs). The first five

181    months are considered as spin-up, while the rest of the data are used for comparison with

182    surface-based observations from Ny-Ålesund. A description of the modeled ice microphysics,

183    which is the main focus of this study, and the implemented modifications follow below.

184       The atmospheric component of NorESM2 is CAM6-Oslo, which consists of the

185    Community Atmosphere Model version 6 (CAM6) and the OsloAero5.3 (Kirkevåg

186    et al. 2018) aerosol scheme. CAM6-Oslo employs the Morrison and Gettelman (2015)

187    microphysics scheme (MG2), which accounts for four hydrometeor types: cloud droplet,

188    raindrop, cloud ice and snow. Heterogeneous PIP parameterizations follow the Classical

189    Nucleation Theory (CNT; Hoose et al. 2010; Wang et al. 2014) which accounts for

190    immersion, contact and deposition freezing of two INP species, dust and soot. Immersion

191    freezing is only allowed to occur below -10$^{o}$C in this scheme for both INP species, while only

192    10% of the soot concentrations are considered efficient INPs. While CNT is the default

193    nucleation scheme used in CMIP6, the model employs an alternative option for PIP: CNT can

194    be replaced by diagnostic parameterizations that are a function of basic thermodynamic

195    variables and do not account for explicit cloud-aerosol interactions. These include the Bigg

196    (1953), Young (1974) and Meyers et al. (1992) parameterizations for immersion, contact and

197  deposition freezing, respectively. The Bigg (1953) and Young (1974) parameterizations are

198  activated at temperatures below -4$^{o}$C, while Meyers et al. (1992) is active within the -37$^{o}$C–

199  0$^{o}$C temperature range.

200      Secondary ice production is accounted in MG2 scheme only through the HM

201  mechanism, which is parameterized following Cotton et al. (1986). This formulation

202  considers a maximum splinter production of 350 splinters per milligram of rime at -5$^{o}$C, while

203  the process efficiency decreases to zero at temperatures below (above) -8$^{o}$C (-3$^{o}$C). However,

204  HM is only activated after cloud droplets collide with snow; in our modified code, we further

205  account for the contribution from raindrop-snow collisions, following Morrison et al. (2005)

206  scheme, using the same parameterization (Cotton et al. 1986) for the prediction of the

207  generated fragments. Estimations of mass and number collision tendencies for raindrop-snow

208  collisions are available in the standard MG2 scheme.

209      To represent the BR mechanism, we implement the parameterization of Phillips et al.

210  (2017a). The process is initiated after snow particles collide with each other or with cloud ice.

211  We assume that the collisions that do not result in sticking (aggregation) at an instant

212  timestep, can bounce to initiate the break-up. Phillips et al. (2017a) is a physically-based

213  parameterization that predicts the number of generated fragments as a function of collisional

214  kinetic energy, while the effect of the colliding particles' size, rimed fraction and ice habit is

215  further accounted. MG2 however does not predict rimed fraction and ice habit. For this

216  reason, in our simulations planar ice particles with a 0.4 rimed fraction are assumed; planar

217  shape accounts for a larger range of shapes and is valid for a wider temperature range, while a

218  high fraction has been shown to give the most optimal results in simulations of polar clouds

219  (Sotiropoulou et al. 2020; 2021a). All generated fragments from this mechanism are added to

220  the cloud ice category.

221      The DSH description follows Phillips et al. (2018) and is initiated after raindrop-INP

222  (immersion freezing), raindrop-snow and raindrop-ice collisions. For ice multiplication due to

223  raindrop-INP and raindrop-cloud ice collisions we utilize the formulation referred as 'mode 1'

224  in Phillips et al. (2018), which concerns the accretion of small particles by more massive

225  raindrops, while for snow-raindrop the 'mode 2' formulation is applied. Mode 1 can generate

226  both tiny and big fragments; the former are added to the cloud ice category, while the latter is

227  considered snow. The new tiny fragments are assumed to have a fixed diameter of 10$^{-5}$ m

228  (Phillips et al. 2018) and a constant ice density of 500 kg m$^{-3}$ (which is the default cloud ice

229  density in the MG2 scheme), while the rest of the colliding rain mass is transferred to snow.

230  Freezing probability in this mode is set to unity and zero, at temperatures below -6$^{\circ}$C and

231  above -3$^{\circ}$C, respectively, while it takes intermediate values at temperatures between -6$^{\circ}$C and

232  -3$^{\circ}$. Similarly, the shattering probability is a function of raindrop size, set to 0 and 1 at sizes

233  smaller than 50 μm and larger than 60 μm, respectively. Mode 2 can only generate tiny

234  fragments. Tiny fragments are added to the cloud ice category, while big fragments are treated

235  as snow.

236  Deshmukh et al. (2022) recently developed an empirical formulation for sublimation

237  break-up of graupel and dendritic snow, in which the total number of the ejected fagments ($N$)

238  is proportional to the square root of the sublimated mass ($M$), $N = K{\cdot}M^{0.57}$, where K is a

239  function of size (diameter) and relative humidity with respect to ice. Since graupel is not

240  accounted in the MG2 scheme, we apply this parameterization to sublimating snow and cloud

241  ice, as long as the diameter for the latter exceeds 200 μm (note that the cloud-ice to snow

242  autoconversion diameter is set to 500 μm in NorESM2). Sublimating cloud ice and snow mass

243  is calculated by the default MG2 scheme. Moreover, since Deshmukh et al. (2022)

244  parameterization is developed based on the observation of dendritic particles, we only allow

245  for sublimation break-up to activate between -10$^{\circ}$C and -20$^{\circ}$C, where such ice habits are more

246  likely to occur in reality (Bailey and Hallet 2009). All new fragments are added to the cloud-

247  ice category. Sublimation break-up of graupel, which is expected to occur at all temperatures

248  (Deshmukh et al. 2022), is not accounted in the model, since graupel is not treated in MG2.

249  Finally, while PIP and SIP are significant ice-crystal sources, aggregation is a critical

250  sink that can substantially decrease the cloud-ice number, while its parameterization is also a

251  source of uncertainty in atmospheric models (Karrer et al. 2021). MG2 scheme accounts for

252  aggregation through cloud ice-snow and snow-snow collisions. The accretion of cloud ice by

253  snow follows the "continuous collection" approach as described in Rutledge and Hobbs

254  (1983), while snow-snow aggregation follows Passarelli (1978). Aggregation efficiency $(E_{ii})$

255  between ice particles is considered the product of collision efficiency and sticking efficiency,

256  with the latter depending on collisional kinetic energy and size (Phillips et al. 2015).

257  However, a very simplified approach for $E_{ii}$ is usually found in climate models; in CAM6-

258  Oslo this parameter is set constant and t to 0.5 (while it was 0.1 in the previous model

259  version).

### c. Sensitivity simulations

261  In this study, we examine the sensitivity of Arctic clouds to three main processes that

262  determine cloud ice number: PIP, SIP and ice aggregation. At this point, it is worth noting

263 that a bug has been recently identified in MG2 (Shaw et al. 2021), which limits ice formation

264 in mixed-phase clouds. This is due to an upper limit ($n_{imax}$) imposed for the ICNCs, which is

265 equal to the INP number. Neither heterogeneous freezing processes nor SIP contribute to this

266 INP limit, preventing them from producing new ice crystals (Shaw et al. 2021). In all our

267 simulations we remove this $n_{imax}$ limit, allowing PIP and SIP to evolve prognostically in the

268 stratocumulus clouds. Our investigations on PIP effects include the use of either the

269 prognostic or the diagnostic treatment for the freezing processes (see section 2*b*). Simulations

270 that employ the Hoose and Möhler (2012) parameterization include the abbreviation 'CNT' in

271 their name, while the ones that are run with diagnostic descriptions (Meyers et al. 1992; Bigg

272 1953; Young et al. 1974) include the prefix 'MBY' (Table 1). The CNT simulation is also

273 referred as 'control' simulation in the text, as this is the model set-up utilized in CMIP6.

274       Sensitivity to SIP descriptions is examined by (a) either accounting for the standard SIP

275 treatment in CAM6-Oslo which includes only the HM process after cloud droplet - snow

276 collisions or (b) activating all the additional mechanisms, described in section 2*b*,

277 simultaneously. Moreover, the performance of SIP processes like BR, which are a function of

278 collisional kinetic energy, can be sensitive to different implementation methods. In this study

279 we examine the performance of bulk vs hybrid-bin descriptions of SIP. Our bulk

280 implementations follow the methodology of Sotiropoulou et al. (2020; 2021a,b) and

281 Georgakaki et al. (2022) for BR and DSH, respectively. In their studies, the characteristic

282 diameters and number-weighted velocities for each hydrometeor are used as input parameters

283 for Phillips et al. (2017a) and (2018) schemes, while the standard MG2 formulations for

284 accretion/aggregation rates are used to estimate the collisions that lead to SIP.

285       However, the MG2 scheme does not account for the accretion of cloud ice on

286 raindrops. To estimate the number and mass collision tendencies for these interactions, we

287 further implement the formulation proposed by Reisner et al. (1998), which is also utilized in

288 the Morrison et al. (2005) scheme. Furthermore, to account for underestimations in collisional

289 kinetic energy when the terminal velocity of the two colliding particles is similar ($u_1 \approx u_2$), we

290 adapt the corrections in the mass- or number-weighted difference in terminal velocity ($\Delta u_{12}$)

291 proposed by Mizuno (1990) and Reisner et al. (1998) in the bulk SIP implementations. When

292 snowflakes collide with each other, it is assumed that 0.1% of the colliding mass is transferred

293 to the generated fragments (Phillips et al. 2017a). The same assumption is applied for mode 2

294 of the drop-shattering process, thus only 0.1% of the colliding mass is transferred to the tiny

295 fragments (Phillips et al. 2018). A detailed description of the implementation method can be

296    found in Sotiropoulou et al. (2021a) and Georgakaki et al. (2022).

297    On the contrary, Zhao et al. (2021) used an emulated bin approach for these two

298    mechanisms, that better accounts for the impact of the size spectra variability. In their

299    framework, the collision rates are calculated for each bin as $E_c\,\delta N_1\,\delta N_2\,\pi\,(r_1+r_2)^2\,|\,u_1\text{-}u_2|$,

300    where $E_c$ is the collision efficiency, and $\delta N_1$ and $\delta N_2$ are the number concentrations in the two

301    bins with particle radiuses $r_1$ and $r_2$, respectively. Similarly, to the bulk approach described

302    above, the number of generated fragments per collision is estimated following Phillips et al.

303    (2017, 2018). Each new fragment produced by these two processes is assumed to have a 10-

304    μm size (Phillips et al. 2018). Sensitivity simulations that account for all SIP mechanisms

305    include the abbreviation 'SIP' in their name (Table I), while if an emulated bin framework is

306    used instead of a bulk description, this suffix is modified to 'SIPBN'.  Note that the emulated

307    bin framework is only tested for BR and DSH; the adapted bin diameter ranges follow Zhao et

308    a. (2020), being from 0.1 to 6.5 mm for raindrops (24 bins) and 0.1 to 50 mm for snow and

309    cloud ice particles (35 bins). Each bin diameter (D) is estimated following $D_{k+1}=CD_k$

310    with C=1.2, discretizing the raindrop and ice particle size range in 24 and 35 bins

311    respectively. A bulk approach is used for HM and sublimation break-up in all simulations.

312    Previous applications of these parameterizations in Arctic conditions (Sotiropoulou et

313    al. 2020; Zhao et al. 2022) has shown that BR is the dominant SIP mechanism. However,

314    Sotiropoulou et al. (2021b) showed that the Phillips et al. (2017a) parameterization is largely

315    sensitive to the  sublimation factor ($\psi$) – a correction factor for ice enhancement due to

316    sublimation included  in the BR formulation (see Appendix A). This factor was induced to

317    account for the fact that the field data (Vardiman, 1978) used to constrain the number of

318    fragments generated by this the prescribed $\psi$ in Phillips et al. (2017a) study is overestimated,

319    leading to underestimation  of the BR efficiency. For this reason we perform two more

320    sensitivity simulations, with both prognostic and diagnostic PIP, with this factor removed

321    from the BR formulation. These  experiments include the suffix 'SIPBN$\psi$' in their name, as

322    they are combined with the more  advanced emulated bin framework.

323    Finally, ice aggregation is another process that has a significant impact on ICNCs but is

324    highly-tuned in climate models. Generally observations from mid-latitudes indicate the

325    presence of two temperature zones that promote aggregation: one around -15°C (Barret et al.

326    2019) associated with enhanced dendritic growth that facilitates the interlocking of the ice

327    crystal branches (Connoly et al. 2012), and a second one close to the melting layer (Lamb and

328    Verlinde 2011), caused by the increased sticking efficiency of melting snowflakes. However,

329  an analysis of recent dual-wavelength radar observations of shallow clouds from Ny-Ålesund

330  suggest that enhanced aggregation occurs between -10$^{o}$C and -15$^{o}$C (Chellini et al. 2022),

331  while no evidence of this process is found at higher temperatures. To adjust the aggregation

332  efficiency to these new findings we perform simulations with modified $E_{ii}$. While in the

333  standard scheme the aggregation efficiency remains constant to 0.5 throughout the whole

334  temperature range, in our sensitivity simulations with the suffix 'AGG' this high value is only

335  sustained between -10$^{o}$C and -15$^{o}$C. At colder temperatures $E_{ii}$ is set to 0.1, while at warmer

336  temperatures aggregation is deactivated ($E_{ii}$=0). A description of all the performed sensitivity

337  tests and the different combinations of PIP, SIP and aggregation treatments is given in Table

338  1.

339

340  **TABLE 1: Description of the sensitivity simulations**

|  | **Primary Ice Production** | **Secondary Ice Production** | **Aggregation** |
|---|---|---|---|
| CNT (CONTROL) | prognostic (CNT) | HM (cloud droplet-snow) | constant $E_{ii}$ |
| MBY | diagnostic (Meyers et al., Bigg , Young ) | HM (cloud droplet-snow) | constant $E_{ii}$ |
| CNT_AGG | prognostic (CNT) | HM (cloud droplet-snow) | variable $E_{ii}$ |
| MBY_AGG | diagnostic (Meyers et al., Bigg, Young) | HM (cloud droplet-snow) | variable $E_{ii}$ |
| CNT_SIP | prognostic (CNT) | HM (cloud droplet/rain-snow), bulk BR, bulk DS, SUBBR | constant $E_{ii}$ |
| MBY_SIP | diagnostic (Meyers et al., Bigg, Young) | HM (cloud droplet/rain-snow), bulk BR, bulk DS, SUBBR | constant $E_{ii}$ |
| CNT_SIPBN | prognostic (CNT) | HM (cloud droplet/rain-snow), bin BR, bin DS, SUBBR | constant $E_{ii}$ |
| MBY_SIPBN | diagnostic (Meyers et al., Bigg, Young) | HM (cloud droplet/rain-snow), bin BR, bin DS, SUBBR | constant $E_{ii}$ |
| CNT_SIPBN$\psi$ | prognostic (CNT) | HM (cloud droplet/rain-snow), bin BR ($\psi$=1), bin DS, SUBBR | constant $E_{ii}$ |
| MBY_SIPBN$\psi$ | diagnostic (Meyers et al., Bigg, Young) | HM (cloud droplet/rain-snow), bin BR ($\psi$=1), bin DS, SUBBR | constant $E_{ii}$ |
| CNT_SIPBN_AGG | prognostic (CNT) | HM (cloud droplet/rain-snow), bin BR, bin DS, SUBBR | variable $E_{ii}$ |
| MBY_SIPBN_AGG | diagnostic (Meyers et al., Bigg, Young) | HM (cloud droplet/rain-snow), bin BR, bin DS, SUBBR | variable $E_{ii}$ |
| CNT_SIPBN$\psi$_AGG | prognostic (CNT) | HM (cloud droplet/rain-snow), bin BR ($\psi$=1), bin DS, SUBBR | variable $E_{ii}$ |

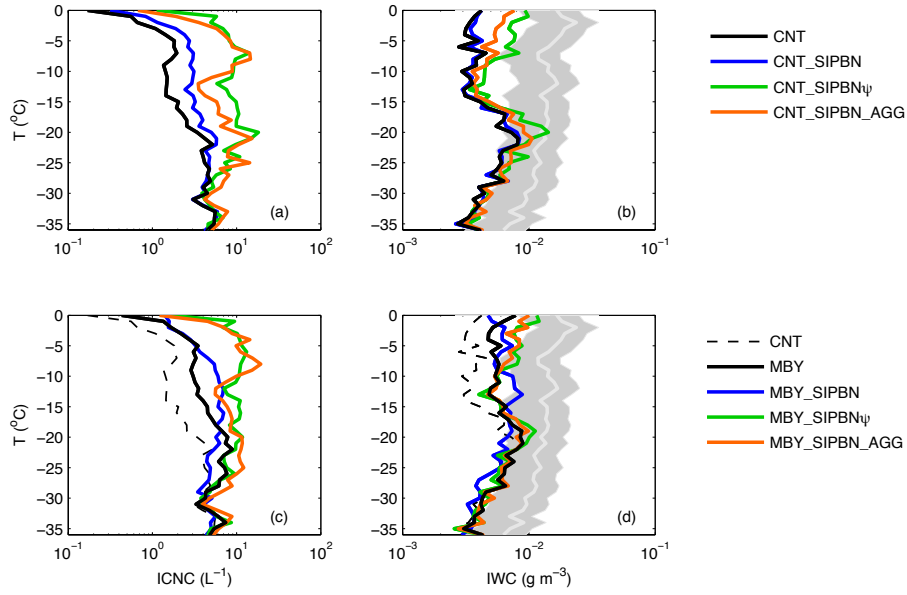| MBY_SIPBNψ_AGG | diagnostic (Meyers et al., Bigg, Young) | HM (cloud droplet/rain-snow), bin BR ($\psi$=1), bin DS, SUBBR | variable $E_{ii}$ |

## 3. Results

### a. Ny-Ålesund site

#### 1) Cloud properties

In this section we focus on the evaluation of the simulated cloud macrophysical properties against remote-sensing surface observations collected at Ny-Ålesund (see section 2*a*). An evaluation of the modeled thermodynamic conditions is presented in Figs. S1 and S2 in the Supporting Information. NorESM2 offers a realistic representation of the temperature (Fig. S1a,b) and IWV (Fig. S2a) fields. Somewhat colder conditions are often found in the model within the lowest first two kilometers of the atmosphere (Fig. S1c), but most of the instantaneous modeled values show a discrepancy lower than $5^{o}$ from the observed (Fig. S1d). In Figure S2, while instantaneous modeled and observed IWV values occasionally show large discrepancies (Fig. S2b), the overall mean observed (modeled) IWV is 7.4 (8.6) kg m$^{-2}$ suggesting a reasonable agreement.

Instantaneous modeled ICNC and IWC values derived at 3-hour time resolution are used in Fig. 1, which presents the median estimates as a function of temperature. ICNCs are constructed from the in-cloud cloud ice number and the in-precipitation snow number, predicted by the model. Similarly, modeled IWC is constructed from the respective in-cloud cloud ice and in-precipitation snow mass mixing ratios. IWC retrievals are averaged over a $\pm$10-minute window around the model output timesteps and within $\pm$20 meters around the model vertical levels, while ICNC measurements are not available at this site. Measurement uncertainty is also plotted in Fig. 1b.

**FIG 1.** (a, c) Ice crystal number concentration (ICNC) and (b, d) ice water content (IWC) as a function of temperature. Grey shading (line) indicate the uncertainty range (50%) in the measured values. Results are derived from the Ny-Ålesund site (grid-point) for the period June 2016- May 2018. The observed IWC values are averaged over a ±10-minute window around the model output timesteps and within ±20 meters round the model vertical levels.

The aerosol-aware CNT (control) simulation produces median ICNC concentrations round 1.5 L$^{-1}$ within the -5$^{o}$C to -15$^{o}$C temperature range (Fig. 1a), which results in a median IWC that is on average five times lower than the observed (Fig. 1b). The IWC discrepancies between CNT and observations are reduced below -15$^{o}$C: the median IWC is only two times lower than the observed median at these cold temperatures and lays very close to the uncertainty range. CNT_SIP does not result in any ice enhancement; for this reason it is shown in the Supplementary Information (Figure S3). CNT_SIPBN results in a weak ICNC enhancement within the temperature range that is favorable for SIP (Fig. 1a), compared to CNT, with hardly any impact on median IWC (Fig. 1b). CNT_AGG produces similar results to CNT_SIPBN (Fig. S3), thus activating SIP or decreasing ice aggregation has a similar effect on ICNCs. CNT_SIPBNψ and CNT_SIPBN_AGG produce similar ICNC enhancements, resulting in 5-15 times larger median values (Fig. 1a) at the relatively high (>-15$^{o}$C) temperatures compared to CNT. Median ICNC values are close to 10 L$^{-1}$ in these two simulations (Fig. 1a), which are in agreement with recent SIP observations from Arctic clouds at Ny-Alesund (Pasquier et al. 2022). Median IWC is 2-3 times larger in CNT_SIPBNψ and CNT_SIPBN_AGG at temperatures above -15$^{o}$C, compared to CNT, in closer agreement with observations (Fig. 1b). CNT_SIPBNψ_AGG, which includes both the modified ψ factor and decreased aggregation results in reasonable agreement with the observed IWC (Fig. S3b),

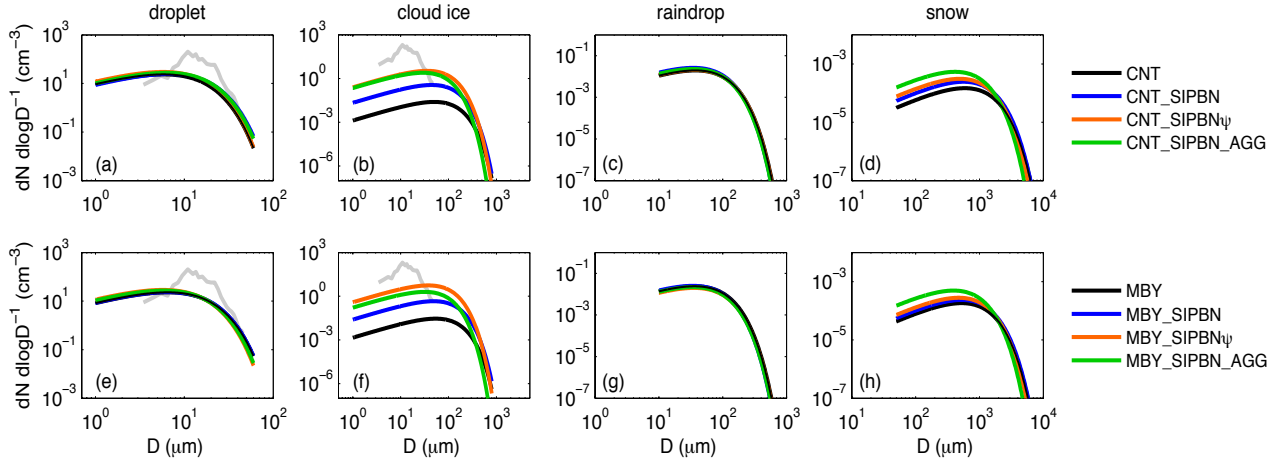390    however median ICNCs exceed 100 L$^{-1}$ (Fig. S3a). Such median values are extreme and have

391    not been observed in the Arctic. Since this set-up results in unrealistic microphysical

392    properties, it is excluded from the rest of the analysis.

393         The MBY simulation (Fig. 1c) produces about 2-2.5 times higher median ICNCs than

394    CNT at temperatures above -15$^{o}$C, which increases median IWC values by 50-80% (Fig. 1d),

395    in slightly better agreement with observations. No improvement in IWC is found at colder

396    temperatures with the diagnostic PIP treatment. MBY_SIPBN results in negligible

397    differentiations compared to the MBY simulation that do not affect the ice macrophysical

398    state of the modeled clouds (Fig. 1d). The same applies for MBY_SIP and MBY_AGG,

399    shown in the supplementary information (Fig. S3). Similarly to CNT_SIPBNψ and

400    CNT_SIPBN_AGG, MBY_SIPBNψ and MBY_SIPBN_AGG produce median ICNCs  close

401    to 10 L$^{-1}$, which are realistic for Arctic SIP conditions observed at Ny-Alesund (Pasquier et al.

402    2022);  these set-ups in somewhat improved IWC at temperatures above -15$^{o}$C. Despite the

403    improved median IWC in MBY_SIPBNψ_AGG (Fig. S3d), this simulation produces

404    unrealistically high median ICNCs (> 100 L$^{-1}$), similar to CNT_SIPBNψ_AGG (Fig. S3a,c).

405    and thus this simulation is also excluded from the following analysis.

406         It is worth noting that CNT_SIPBN_AGG (MBY_SIPBN_AGG) is substantially more

407    efficient in ICNC enhancement than CNT_SIPBN (MBY_SIPBN) and CNT_AGG

408    (MBY_AGG), which are more similar (Fig. S3). This indicates an important interplay

409    between SIP and decreased ice aggregation, when combined together. An overestimated

410    aggregation rate can substantially limit ice multiplication, as the new fragments will rapidly

411    aggregate and form precipitation-sized particles that will lead to IWC depletion through

412    sedimentation (not shown). It is worth noting that the worst CNT_SIPBN_AGG and

413    MBY_SIPBN_AGG  performance is found at temperatures between -10$^{o}$C and -15$^{o}$C, where

414    the default aggregation efficiency remains unaffected (see section 2$c$). This suggests that

415    constraining ice aggregation is critical for the representation of Arctic cloud properties,

416    particularly in conditions that favor SIP.

417         ICNC measurements were not conducted at Ny-Ålesund in 2016-2018, thus the ICNC

418    profiles presented in Fig. 1 cannot be evaluated against observations. Only measured cloud

419    particle concentrations over a limited size range (<50 μm) collected with the CVI and the FM-

420    120 monitor are available (see section 2$a$). The FM-120 measurements are shown in Fig. 2

421    along with the modeled in-cloud droplet and cloud ice size spectra that include the sampled

422    size range. Size spectra of larger particles, rain and snow are also shown in the same figure to

423  give a complete overview of the microphysical differences between the different simulations.

424  The spectral differences between the standard NorESM2 set-up (CNT or MBY) and the

425  sensitivity simulations are further highlighted in Fig. S4.

426



427

**FIG 2.** (a, e) droplet, (b, f) cloud ice, (c, g) raindrop and (d, h) snow size distributions for the different model sensitivity simulations. The first (second) row of panels presents simulations conducted with prognostic (diagnostic) PIP. Grey lines in panels (a, e) and (b, f) represent the observed spectrum derived from the fog monitor FM-120 for the size range 3.5-46 μm. All data span the period June 2015 - February 2018, as cloud particle measurements were not collected beyond this date.

433

434  All model simulations underestimate the measured hydrometeor concentrations at  sizes

435  between 10-30 μm. Differentiations in liquid hydrometeors among the simulations are

436  generally small (Fig. 2a,c,e,g), while the set-ups that significantly enhance ICNCs  in Fig. 1

437  produce more droplets within the 1-10 μm size range. More pronounced differences among

438  the simulations are found in the cloud ice particle spectra: increasing ice production (Fig. 1)

439  substantially enhances the smaller particles (Fig. 2b, f) in CNT_SIPBNψ,

440  CNT_SIPBN_AGG, MBY_SIPBNψ and MBY_SIPBN_AGG simulations. This improves the

441  agreement with observations particularly within the 10-30 μm size range, where CNT and

442  MBY produce the largest cloud-ice underestimations. CNT_AGG (MBY_AGG) and

443  CNT_SIP (MBY_AGG) are not included in Fig. 2, as they produce very similar spectra to

444  CNT (MBY) and CNT_SIPBN (MBY_SIPBN), respectively. Distinct differences are also

445  found in the snow size spectra (Fig. 2d, h) , with the most pronounced shifts towards smaller

446  snowflakes produced by simulations with reduced aggregation. This is however expected as

447  aggregation directly augments the mass of snow particles either through self-collection or

448  collection of cloud ice. Differences in the rain spectra are not pronounced (Fig. 2d, h):

449  simulations with modified SIP or/and aggregation generally produce somewhat larger

15

450 raindrop concentrations compared to the default set-up (Fig. S4c, g), albeit these deviations

451 are small in magnitude.

452    Overall, the large concentrations of the small particles measured at Zeppelin Station are

453 not produced by any simulation. Atlas et al. (2021) have previously shown similar deviations

454 between the default CAM6 and cloud particle measurements within the 5-30 μm size range,

455 conducted with cloud probes, in high-latitude mixed-phase stratocumulus conditions

456 (Southern Ocean clouds in their case). However, in our study the addition of missing SIP

457 mechanisms did not eliminate this discrepancy. Another fact that may affect our model's

458 performance is that it does not account for blowing snow, a mechanism that is commonly

459 observed in mountainous regions and is known to provide the clouds with small ice particles

460 raised from the surface during windy conditions *(Gossart et al. 2017)*.

461    Apart from the cloud measurements collected on mount Zeppelin, insights into the

462 particle sizes can be obtained from the radar-retrieved $r_{ieff}$. However, this dataset is associated

463 with large uncertainties (see section 2*a*). The retrievals result in a median $r_{ieff}$ of 44 μm for

464 measurements collected above -20$^o$C. This value is 79.8 μm for CNT and 79.3 μm for MBY

465 and somewhat decreases in simulation with increased ice production. Among the simulations

466 that utilize CNT PIP scheme, shown in Figs 1 and 2, CNT_SIPBN_AGG produces the median

467 $r_{ieff}$ closest to the observed (67.8 μm), while among the simulations with the diagnostic PIP,

468 MBY_SIPBNψ produces the smaller radii  (64.5 μm). However, the differences in the

469 modeled $r_{ieff}$  do not exceed ~15 μm between the different model set-ups, which is

470 substantially smaller than the uncertainty in the $r_{ieff}$ retrieval, indicating these measurements

471 cannot be used for a robust microphysical evaluation.

472    LWP measurements exhibit considerable variability throughout the year; for this

473 seasonal LWP statistics are presented in Table 2. Moreover, as LWP distribution appears

474 highly skewed, especially during winter and spring, both mean and median values are

475 included in the Table. Observational statistics are also included in Table 2, derived from LWP

476 measurements interpolated at the model timesteps. Modeled  in-cloud LWP is constructed

477 from the cloud droplet mixing ratios. Outliers with in-cloud LWP values > 700 g m-2 are

478 excluded from the analysis. Moreover, for a consistent comparison with the processed

479 observations,  modeled cases with liquid surface precipitation >. 0.05 mm day$^{-1}$ (Kiszler et al.

480 2023) are also discarded from the LWP statistics.

481    Simulations with CNT produce generally more LWP than those that utilize the

482 diagnostic PIP scheme. All simulations substantially overestimate LWP in summer, while

activation has minor impact on the mean/median values. In contrast, activation of SIP in simulations with diagnostic PIP has more pronounced effects: MBY_SIPBNψ and MBY_SIPBN_AGG produce the lowest LWP values in summer, in better agreement with observations, although still overestimated. MBY simulation produces a somewhat better LWP in autumn compared to CNT, as it only deviates only ~10 g m$^{-2}$ (~22 g m$^{-2}$) from the mean (median) observed value. Activation of SIP in the simulations with prognostic PIP has weak impact on LWP statistics, as the differences in mean values are smaller than 5 g m$^{-2}$ compared to CNT. On contrary, SIP impacts are more pronounced in the simulations with diagnostic PIP, as increasing ice production results in decreasing mean/median LWP in autumn. MBY overestimates the observed mean/median LWP by ~ 11/22 g m$^{-2}$, while MBY_SIPBN and MBY_SIPBNψ exhibit a very good agreement with observations.

CNT overestimates mean LWP in winter by ~20 g m$^{-2}$, while MBY produces in-cloud values very similar to the observed. Activation of SIP in simulations that treat PIP through CNT results in dereased LWP and improves agreement with observational statistics. In particular, CNT_SIPBNψ (CNT_SIPBN_AGG) gives the best representation of the mean (median) winter LWP. In contrast, enhanced ice production through SIP in MBY_SIPBNψ produces underestimated LWP compared to MBY, leading to larger deviations from the observations. MBY_SIPBN and MBY_SIP_AGG only slightly differentiate from MBY. Finally, model performance in spring for LWP is similar to winter: CNT overestimates LWP (albeit the deviations are less pronounced than for summer and autumn seasons), while increasing ice production in CNT_SIPBN and CNT_SIPBN_AGG improves agreement with measurements, with CNT_SIPBN being more realistic in this season. On contrary, mean and median LWP in MBY and MBY_SIP set-ups is very close to the observed spring values, while increasing ice production in MBY_SIPBN and MBY_SIPBN_AGG results in underestimated cloud liquid

**TABLE 2:** in-cloud Liquid Water Path (LWP, g m$^{-2}$) for observations and sensitivity simulations, segregated into mean/median seasonal values.
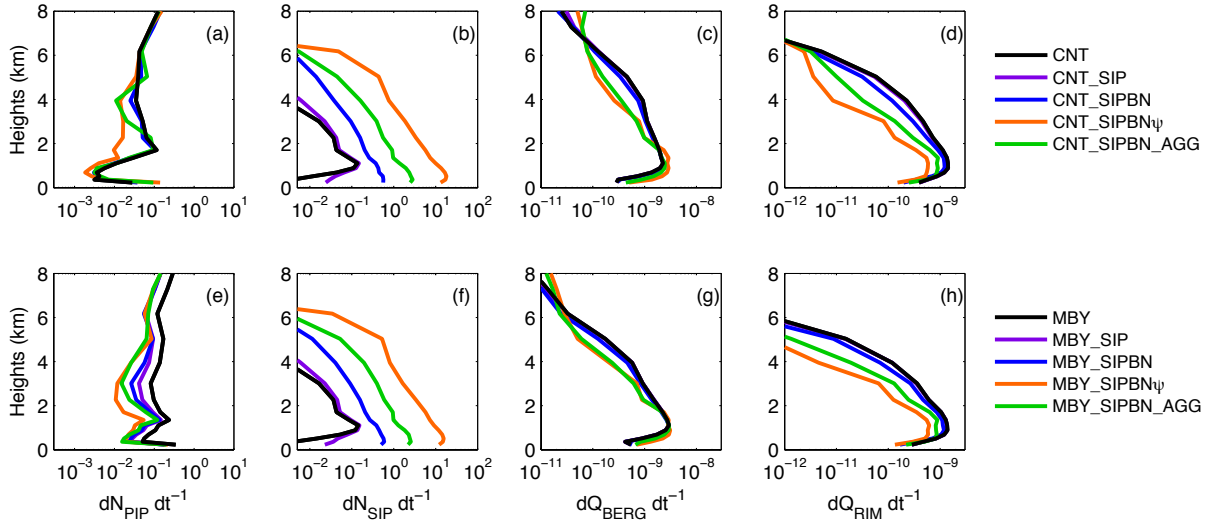
|  | **summer** | **autumn** | **winter** | **spring** |
|---|---|---|---|---|
| **Observations** | **83.6/ 39.8** | **81.1/ 23.6** | **34.7/ 2.7** | **38.3/ 2.9** |
| CNT (CONTROL) | 135.2/ 116.4 | 99.1/ 57.3 | 54.7/ 5.9 | 58.1/ 10.6 |
| CNT_SIPBN | 141.6/ 120.6 | 101.4/ 61.9 | 52.8/ 4.2 | 58.6/ 7.9 |

17

| | | | | |
|---|---|---|---|---|
| CNT_SIPBN$\psi$ | 134.3/ 115.0 | 94.3/ 54.6 | 26.1/ 5x10$^{-5}$ | 45.2/ 5.9 |
| CNT_SIPBN_AGG | 136.6/ 116.0 | 103.1/ 63.5 | 46.7/ 3.3 | 53.7/ 7.4 |
| MBY | 126.4/ 108.5 | 91.6/ 55.5 | 33.6/ 3.6 | 37.3/ 5.5 |
| MBY_SIPBN | 129.8/ 107.2 | 81.8/ 36.8 | 32.9/ 3.3 | 39.4/ 4.7 |
| MBY_SIPBN$\psi$ | 119.1/ 97.4 | 78.7/ 32.9 | 17.5/ 4x10$^{-5}$ | 27.2/ 2.0 |
| MBY_SIPBN_AGG | 118.9/ 95.5 | 62.5/ 12.5 | 30.9/1.15 | 29.9/ 4.1 |

511

## 2) Microphysical processes

To better understand the interactions between the underlying microphysical processes that drive the macrophysical differences between the different sensitivity simulations, vertical profiles of mean PIP, SIP, WBF and riming tendencies are plotted in Fig. 3. The ice multiplication tendencies of the individual SIP mechanisms are shown in Fig. 4. Interestingly, when a diagnostic PIP treatment is applied (Fig. 3e), PIP rates generally decrease with increasing ice production through modifications in SIP or aggregation, a behavior that is not found in simulations with CNT (Fig. 3a). An analysis of the changes in thermodynamic profiles between the simulations (Fig. S5a, c) indicate warmer temperatures with increasing ice production, especially at heights above 1 km, while the specific humidity response is more variable (Fig. S5b, d); since the diagnostic PIP parameterizations are solely dependent on the thermodynamic conditions, these temperature variations can explain to a large extent the variable PIP rates in Fig. 3e. In Fig. 3a substantial differences in PIP are mainly found in CNT_SIPBN$\psi$; these differences seem to follow changes in specific humidity profiles (Fig. S5b, d) suggesting that the prognostic PIP treatment is mostly affected by variations in supersaturation.

SIP rates in CNT_SIP and MBY_SIP are very similar to CNT and MBY (Fig. 4b, f). This is in agreement with the findings of Fig. S1, which reveal that the bulk implementations of BR and DSH hardly result in any ice multiplication. This result is further confirmed by Fig. 4 which shows that BR and DSH tendencies are orders of magnitude smaller than those of HM. Another interesting finding is that including rain-snow collisions in the HM description in the CNT_SIP and MBY_SIP simulations does not enhance the efficiency of this process compared to CNT and MBY that account only for cloud drop-snow collisions (Fig. 4a, e), as the precipitation particle concentrations are generally limited (Fig. 2c,d,g,h). Furthermore, sublimation breakup activates in the lowest five atmospheric kilometers but remains extremely weak through the whole layer (Fig. 4d, h).
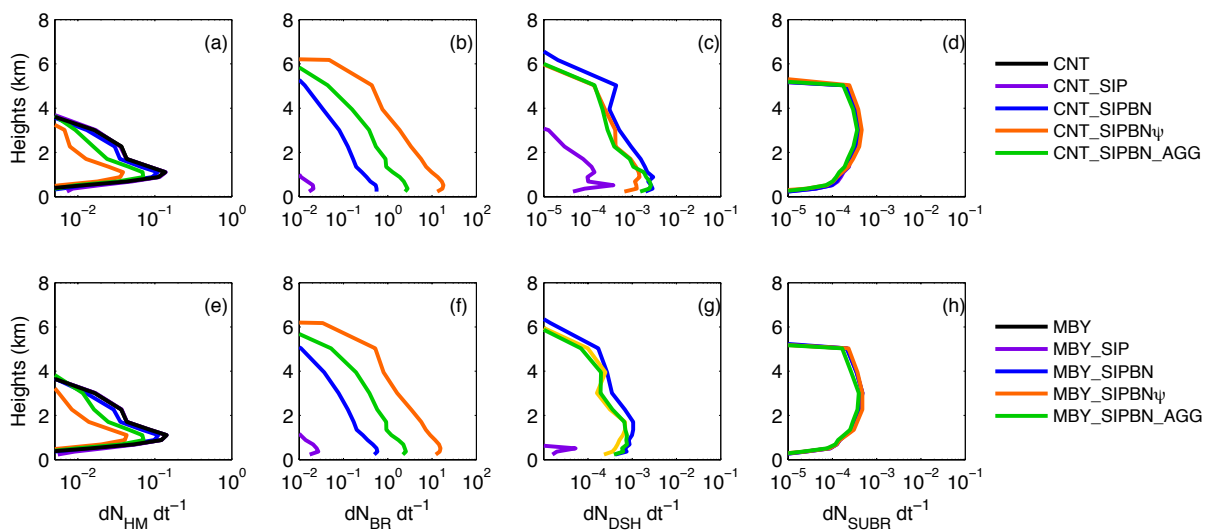
18

**FIG 3.** Mean vertical profiles of number concentration tendencies ($kg^{-1}$ $s^{-1}$) due to (a, e) PIP ($dN_{PIP}$ $dt^{-1}$) and (b, f) SIP ($dN_{SIP}$ $dt^{-1}$), (c, g), and mass concentration tendencies (kg $kg^{-1}$ $s^{-1}$) due to WBF ($dQ_{BERG}$ $dt^{-1}$) and (d, h) riming ($dQ_{RIM}$ $dt^{-1}$) for the different model sensitivity simulations. The WBF rate is the sum of the individual rates for cloud ice and snow particles, while riming is the sum of cloud droplet and rain accretion on snow. The first (second) row of panels presents simulations conducted with prognostic (diagnostic) PIP.

Utilizing an emulated bin framework for BR and DSH enhances SIP rates by on average a factor of ~5 in the lowest 4 atmospheric kilometers, compared to the simulations that adapt bulk frameworks (Fig. 3b, f). SIP also becomes prominent at higher altitudes (> 4 km), where bulk parameterizations do not produce any ice multiplication. Figure 4 indicates that the SIP is mainly due to the BR process. Although the emulated bin framework enhances DSH efficiency, the DSH rates remain substantially lower than those that correspond to the BR mechanism. Decreasing aggregation in CNT_SIPBN_AGG and MBY_SIPBN_AGG increases SIP efficiency by on average a factor of 5 (Fig. 3b, f), compared to CNT_SIPBN and MBY_SIPBN simulations, mainly through the enhancement of the BR process (Fig. 4b, f). Interestingly, the largest sensitivity of SIP is found in the treatment of the sublimation correction factor $\psi$ in BR description. The simulation with $\psi=1$ (Table 1), that does not account for this correction results in BR rates enhanced by 1-1.5 orders of magnitude (Fig. 4b,f), which highlights the importance of constraining this parameter for an accurate BR representation. It is worth noting that increasing BR efficiency is associated with decreasing HM rates (Fig. 4). This is due to the fact that increasing SIP results in smaller ice particle sizes that are less likely to rime and initiate HM. The impact of SIP on riming and the WBF

563 efficiency will be discussed below.

564      The simulations with a modified $\psi$ factor or aggregation efficiency are characterized by

565 an enhanced (reduced) WBF efficiency in the low-level (mid-level) clouds (Fig. 3c, g)

566 compared to the rest of the simulations that produce significantly less ice content (Fig. 1).

567 These simulations are also characterized by decreased riming efficiency throughout the whole

568 troposphere (Fig. 3d, h). This is likely due to the shift of the frozen hydrometeor spectra to

569 smaller particle sizes (Fig. 2) that are less efficient in depositional growth and liquid

570 accretion. The more active WBF mechanism in the low-level clouds is likely responsible for

571 the reduced in-cloud LWPs (Table 2).

572      Our findings indicate that the inclusion of missing SIP mechanisms in NorESM2 can

573 improve the macrophysical representation of Arctic mixed-phase clouds, but this requires the

574 use of an emulated bin framework for BR and DSH, which is computationally about two

575 times more demanding than the bulk descriptions of SIP. Modifications in the HM

576 description, with the inclusion of rain-snow interactions, did not enhance the efficiency of this

577 process in the examined conditions, suggesting that these modifications are redundant. BR

578 appears to be the dominant SIP mechanism, however its efficiency is very sensitive to the

579 treatment of the poorly constrained parameter $\psi$. DSH and SUBR processes are substantially

580 weaker in the examined conditions. DSH is likely not favored due to lack of relatively large

581 drops to initiate the process (Fig. 2c, g), while SUBBR is likely limited by the high relative

582 humidity conditions that generally dominate in the Arctic.

583

584



585 **FIG 4.** Mean vertical profiles of number concentration tendencies (kg$^{-1}$ s$^{-1}$) due to SIP from the (a, d)

586 HM, (b, f) BR and (c, f) DSH and (d, h) SUBBR for the different model sensitivity simulations. The

587     first (second) row of panels presents simulations conducted with prognostic (diagnostic) PIP.

588

589     *b. Arctic region*

590     In this section, the performed simulations are evaluated against satellite observations averaged

591     over the whole Arctic region (>66°N). In Table 3 the simulated net total cloud radiative

592     effects (CRE) at the Top Of the Atmosphere (TOA) are compared to EBAF v4.1 products;

593     differences in the net surface cloud radiative effect are found less significant and thus are not

594     shown. Furthermore, in Table 4 the modeled and observed total cloud cover is presented; the

595     latter is represented by the GOCCP product. Two values are shown for the different

596     simulations: (a) the COSP (CFMIP Observation Simulator Package) output which is suitable

597     for comparison with the satellite observations (Bodas-Salcedo et al. 2011) and (b) the direct

598     model outputs, which control radiation (Table 4).

599     Net CRE at TOA is negative in summer and spring, as shortwave effects dominate,

600     while during autumn-winter, when incoming solar radiation is weaker, the dominance of the

601     longwave components result in positive values. The simulations that utilize the CNT PIP

602     scheme produce enhanced warming (cooling) at TOA autumn-spring (summer) than the

603     simulations with diagnostic PIP parameterizations, resulting in slightly better (worse)

604     agreement with EBAF observations. CNT overestimates cloud radiative cooling at TOA in

605     summer by 5.3 W m$^{-2}$ and overestimates cloud induced warming during the rest of the

606     seasons, with the largest deviations from EBAF observations found in winter (4.6 W m$^{-2}$).

607     CNT_SIPBN produces very similar results to CNT, while the two simulations with the

608     enhanced ice production produce larger net longwave effects (Table S1), shifting the net CRE

609     towards warmer values. This improves the representation of the net cloud radiative effect

610     during most of the year, with the largest improvements found in winter for

611     CNT_SIPBN_AGG (~3 W m$^{-2}$). Differences in shortwave CRE at TOA among the

612     simulations are generally smaller, never exceeding 1.5 W m$^{-2}$ (Table S2). The response of the

613     simulations with diagnostic PIP to increasing ice production is similar to those that employ

614     CNT, but weaker in magnitude. As a result, the differences between MBY and

615     MBY_SIPBN_AGG or MBY_SIPBNψ are generally small (<1.5 W m$^{-2}$). The most

616     pronounced improvement in net CRE is found in simulation MBY_SIPBNψ for the summer

617     season, however this is due to compensating errors between the shortwave and longwave

618     components (Tables S1, S2).

619

620     **TABLE 3**: Net Total Cloud Radiative Forcing at TOA

|  | summer | autumn | winter | spring |
|---|---|---|---|---|
| **EBAF observations** | **-44.6** | **6.6** | **12.4** | **-7.1** |
| CNT (CONTROL) | -49.9 | 5.3 | 7.8 | -1.9 |
| CNT_SIPBN | -49.1 | 5.3 | 7.9 | -1.8 |
| CNT_SIPBN_AGG | -48.5 | 7.5 | 10.8 | -1.6 |
| CNT_SIPBNψ | -47.6 | 6.2 | 8.6 | -1.2 |
| MBY | -46.7 | 4.6 | 7.7 | -0.8 |
| MBY _SIPBN | -46.1 | 4.7 | 7.8 | -0.7 |
| MBY_SIPBN_AGG | -46.5 | 4.8 | 8.4 | -0.8 |
| MBY_SIPBNψ | -45.3 | 4.8 | 8.4 | -0.5 |

621

622    COSP total cloud cover for CNT and MBY simulations is in good agreement with EBAF
623    observations in summer (Table 4), but underestimates cloud cover during the rest of the
624    seasons, especially in winter and spring.   Increasing ice production result in somewhat
625    increased total cloud cover: the difference between CNT (MBY) and the simulation that
626    produces the largest ice content, CNT_SIPBNψ (MBY_SIPBNψ), is about 1-1.5% (1-4%).
627    Increasing COSP cloud cover is mainly caused by increased high cloud cover (Tables S4);
628    COSP mid-level cloud cover exhibits little sensitivity to variations in ice treatment (not
629    shown), while COSP low-level cloud cover decreases with increasing ice production (Table
630    S3). However, this behaviour is not found in the direct model output, in which both total and
631    low-level cloud cover increase in the simulations with enhanced ice content (Table S3). A
632    possible explanation for this discrepancy is that as the enhanced ice production results in
633    optically-thinner layers, thus the fraction of the very thin clouds that do not pass the detection
634    thresholds applied in the COSP simulator increases (e.g. only subcolumns generated by COSP
635    per model grid with an optical depth > 0.3 are included in the calculations). The direct model
636    outputs however are generally compatible with changes in $CRE_{LW}$ at TOA (Table S1), as
637    increasing cloud cover reduces outgoing thermal radiation, resulting in a warming effect.

638

639    **TABLE 4:** COSP /model total cloud cover. First value is derived from COSP simulator,
640    while the second one corresponds to the direct model output.

|  | summer | autumn | winter | spring |
|---|---|---|---|---|

| EBAF observations | 80.7 | 79.6 | 63.3 | 70.3 |
|---|---|---|---|---|
| CNT (CONTROL) | 81.5/ 85.0 | 75.6/ 85.6 | 57.8/ 78.0 | 55.4/ 74.7 |
| CNT_SIPBN | 81.5/ 85.0 | 75.2/ 85.5 | 57.6/ 78.0 | 54.8/ 74.6 |
| CNT_SIPBN_AGG | 82.3/ 85.7 | 75.7/ 86.3 | 57.6/ 79.0 | 54.7/ 75.5 |
| CNT_SIPBNψ | 82.6/ 86.1 | 75.7/ 86.8 | 57.0/ 79.2 | 53.9/ 75.5 |
| MBY | 79.7/ 83.8 | 69.8/ 83.7 | 50.7/ 76.7 | 46.4/ 71.5 |
| MBY _SIPBN | 79.7/ 83.8 | 69.7/ 83.9 | 60.0/ 76.9 | 46.2/ 71.5 |
| MBY_SIP_AGG | 80.4/ 84.5 | 70.3/ 84.6 | 52.2/ 78.1 | 47.0/ 72.4 |

## 4. Discussion

In this study, we examine the sensitivity of Arctic cloud properties to the representation of ice microphysical processes in NorESM2. The primary target is to quantify the impact of PIP and SIP parameterizations on the cloud macrophysical structure and radiative effects. Sensitivity simulations with PIP are performed with two different primary ice treatments: (a) a prognostic CNT scheme that explicitly predicts ice formation from cloud-aerosol interactions and (b) diagnostic temperature-dependent parameterizations for all the heterogeneous freezing processes. The standard version of NorESM2 accounts only for the HM process through droplet-snow collisions. The sensitivity to SIP is examined by implementing additional SIP mechanisms, namely the BR, DSH and SUBBR mechanisms. Furthermore, the HM description is modified to account for rain-snow collisions, following Morrison et al. (2005).

The interactions of PIP and SIP with ice aggregation are also a subject of the present study. The standard parameterization of this process in NorESM2 includes a constant aggregation efficiency ($E_{ii}$) set to 0.5. To investigate the sensitivity of our results to this parameter, we adapt a variable $E_{ii}$ which is qualitatively constrained by recent dual-wavelength radar measurements of shallow Arctic clouds (Chellini et al. 2022): $E_{ii}$ is set to 0.5 at temperatures between -10$^{o}$C and -15$^{o}$C and to 0 (0.1) at temperatures below (above) this range. The model results are evaluated against surface observations from Ny-Ålesund and satellite retrievals over the whole Arctic.

Using CNT instead of diagnostic PIP descriptions results in a worse agreement with IWC observations from Ny-Ålesund at temperatures between -5$^{o}$C and -15$^{o}$C, when no other modification in SIP or aggregation is implemented. We speculate that the reason for this behavior is that the NorESM2 CNT parameterization does not account for aerosol types that

23

674      are efficient INPs at relatively warm temperatures (e.g. biological aerosols). This larger

675      underestimation in ice content is accompanied by substantially overestimated LWP, compared

676      to the observed.

677          Activating the missing SIP mechanisms enhances ice content, mainly through the BR

678      process. BR efficiency however highly depends on the treatment of the correction factor $\psi$,

679      which is included in the Phillips et al. (2017a) parameterization to account for the ice

680      enhancement due to sublimation. This is a poorly constrained parameter, while the value

681      assigned by Phillips et al. (2017a) likely results in underestimations of the BR effect. DSH

682      and SUBBR are the two mechanisms with the weakest efficiency in the examined conditions.

683      Moreover, modifications in the HM description to account for rain-snow collisions do not

684      enhance the efficiency of the process. HM and DSH are likely limited by the fact that

685      relatively large raindrops are generally few in the examined conditions. SUBBR is likely not

686      favored due to the high relative humidity conditions (Wyszyński and Przybylak 2014;

687      Tjernström et al. 2012) that often persist in polar environments.

688          It is worth noting that the current BR and SUBBR implementations can be affected by

689      the number of frozen hydrometeors that are treated in the cloud scheme and MG2 does not

690      account for graupel particles. While Gettelman et al. (2019) showed that the global climate

691      impact of rimed ice in stratiform clouds is negligible in 100-km scale simulations, their study

692      concerns the standard MG2 scheme that does not account for additional SIP mechanisms.

693      Zhao et al. (2020, 2021) on the other hand showed that including graupel can enhance the

694      efficiency of the BR process in Arctic clouds. Similarly, the SUBBR implementation

695      concerns only the snow particles in our model, which can undergo sublimation break-up only

696      within a limited temperature range (see Section 2c). In contrast, sublimation break-up of

697      graupel can occur at any temperature (Deshmukh et al. 2022). In summary, the fact that

698      graupel category is not treated in NorESM2 suggests that the overall efficiency of both BR

699      and SUBBR mechanisms might be underestimated in our simulations.

700          Interestingly, SIP efficiency increases substantially with decreasing ice aggregation in

701      our simulations. This is because enhanced SIP results in enhanced ice aggregation when a

702      constant aggregation efficiency is assumed. However, in reality, this might not be necessarily

703      true as enhanced SIP may lead to the prevalence of small ice particles that are not efficient in

704      aggregation or to the reduction of dendritic ice crystal concentrations through break-up;

705      dendrites are the ice habits that are known to be most favorable for aggregation (Karrer et al.,

706      2021; Chellini et al., 2022).

707  Increasing ice production through changes in SIP and /or aggregation decreases has a

708 direct impact on other microphysical processes, such as riming and WBF efficiency.

709 Specifically simulations with higher ice number are characterized by decreased riming

710 throughout the whole vertical profile. In contrast, WBF exhibits a more variable behaviour: it

711 is less efficient in mid-level clouds, while in low-level clouds below 1-km WBF can become

712 more effective in these simulations. The net effect of all these microphysical processes on the

713 macrophysical structure of the Arctic  clouds at Ny-Alesund site is an enhancement in IWC

714 and reduction in cloud liquid, albeit the latter is more pronounced in simulations with

715 diagnostic PIP. This improves the agreement of the simulations that utilize the CNT PIP

716 scheme with the field observations especially in winter/spring, as CNT is generally

717 characterized by substantially overestimated LWP. In contrast, SIP enhancement or decreased

718 aggregation often results in degraded cloud liquid representation in the simulations with the

719 diagnostic PIP scheme.

720  Finally, as far as SIP/aggregation impacts on cloudiness over the whole Arctic region

721 are concerned, increasing ice production is found to lead to increased total cloud cover.  This

722 is mainly due to the fact that these ice microphysical processes shift the overall cloud ice

723 particle spectra towards smaller sizes, extending the cloud particle lifetime in the atmosphere.

724 The largest increases are observed in the modelled low-level cloud cover; weaker increases

725 are found in the high-cloud cover, while mid-level clouds are hardly impacted. The increased

726 cloudiness, results in improved CRE predictions at TOA especially during the cold months,

727 through improvements mainly in the longwave component. The latter is due to enhanced

728 downward longwave emission, which decreases the negative CRE bias that is produced by the

729 standard NorESM2 model in winter.

730

731 **5. Conclusions**

732 The main objective of this study is to quantify the sensitivity of the Arctic cloud

733 microphysical and radiative properties to the description of three ice microphysical processes

734 (PIP, SIP and ice aggregation) and infer the process hierarchy based on their importance.

735 Changes in PIP treatment have a very pronounced impact on cloud characteristics and

736 radiative impacts, however without the inclusion of missing SIP mechanisms, no PIP scheme

737 alone can reproduce a realistic microphysical structure. The fact that the most realistic

738 simulations include modifications in SIP highlights the importance of this process for

739 modeling Arctic clouds. Yet, SIP representation remains highly sensitive to uncertainties in

740 the description of the underlying mechanisms and particularly collisional break-up. Finally
741 changes in ice aggregation efficiency have very pronounced impacts in our simulations,
742 however this is mainly due to the impact of this process on collisional break-up efficiency,
743 rather than due to its direct impact on the ice/snow budget. Our results suggest that improving
744 SIP representation in climate models can have pronounced impacts on the Arctic cloud
745 representation and cloud radiative effect, especially during winter, however uncertain
746 parameters (such as the correction factor $\psi$ or Eii that affect collisional break-up efficiency)
747 should be constrained or tuned carefully.

748

762

763 **Data availability statement:**
764 Both surface-based and satellite observations are available online. LWP datasets from Ny-
765 Ålesund for the years 2016, 2017 and 2018 can be found at
766 https://doi.org/10.1594/PANGAEA.902096 (Nomokonova et al. 2019a),
767 https://doi.org/10.1594/PANGAEA.902098 (Nomokonova et al. 2019b) and
768 https://doi.org/10.1594/PANGAEA.902099 (Nomokonova et al. 2019c). IWC and Ri$_{eff}$ data
769 can be found at https://doi.pangaea.de/10.1594/PANGAEA.898556 (Nomokonova et al.
770 2019d). HATPRO temperature profiles can be downloaded from
771 https://doi.org/10.1594/PANGAEA.902145 (Nomokova et al. 2019e),
772 https://doi.org/10.1594/PANGAEA.902146 (Nomokova et al. 2019f) and

773  https://doi.org/10.1594/PANGAEA.902147 (Nomokova et al. 2019g). Ny-Ålesund IWV

774  measurements for the same years are available at https://doi.org/10.1594/PANGAEA.902140

775  (Nomokonova et al. 2019h), https://doi.org/10.1594/PANGAEA.902142 (Nomokova et al.

776  2019i) and https://doi.org/10.1594/PANGAEA.902143 (Nomokova et al. 2019j). Cloud

777  measurements collected on mount Zeppelin are available at https://doi.org/10.17043/zeppelin-

778  cloud-aerosol-1 (Karlsson et al. 2021b). The CERES-EBAF data are retrieved from

779  https://ceres.larc.nasa.gov/data/, while GOCCP  dataset can be downloaded from

780  https://climserv.ipsl.polytechnique.fr/cfmip-obs/. ERA-Interim reanalysis products can be

781  accessed through https://www.ecmwf.int/en/forecasts/datasets/reanalysis datasets/era-interim.

782  Model datasets will be deposited to zenodo.org upon acceptance of the manuscript.

783

784  **Appendix A: Sublimation corrector factor in BR formulation**

785  The Phillips et al. (2017a) parameterization predicts the number of fragments ($F_{BR}$) generated

786  from mechanical break-up upon collisions of two ice particles using the equation:

787  $$F_{BR} = \alpha A \left( 1 - exp\left\{ - \left[ \frac{CK_o}{\alpha A} \right]^{\gamma} \right\} \right)$$

788  where $K_o$ is the collisional kinetic energy, $\alpha$ is the surface area of the smaller ice particle that

789  undergoes fracturing, $A$ represents the number density of the breakable asperities in the region

790  of contact, $\gamma$ is a function of the particle's rimed fraction and $C$ is the asperity-fragility

791  coefficient, which is a function of a correction term ($\psi$) for the effects of sublimation based on

792  the field observations by Vardiman (1978). Specifically, for planar ice the assigned values

793  are: $C = 7.08 \times 10^6 \psi$ and $\psi = 3.5 \times 10^{-3}$. Thus, a $\psi$ value smaller than unity has a decreasing

794  impact on $F_{BR}$ estimation. Setting $\psi = 1$ in the sensitivity simulations with '$\psi'$' suffix assumes no

795  impact of sublimation break-up on the Vardiman (1978) data used to constrain the above

796  formulation.

797

798  **References:**

799

800  Atlas, R. L., C.. S Bretherton,., P.N. Blossey, A. Gettelman, C. Bardeen, P. Lin, and Y. Ming,

801  2020: How well do large-eddy simulations and global climate models represent observed

802  boundary layer structures and low clouds over the summertime Southern Ocean? *J.*

803  *Adv. Moeld. Earth Syts*, **12**, e2020MS002205. doi: 10.1029/2020MS002205

804

805 Bacon, N. J., B. D. Swanson, M. B. Baker, and E. J. Davis, 1998: Breakup of levitated frost
806 particles. *J. Geophys. Res.*, **103**, 13 763–13 775, doi: 10.1029/98JD01162.

807

808 Bailey, M. P., and J. Hallett, 2009: A comprehensive habit diagram for atmospheric ice
809 crystals: Confirmation from the laboratory, AIRS II, and other field studies. *J. Atmos.*
810 *Sci.*, **66**, 2888–2899, doi:10.1175/2009JAS2883.1.

811

812 Barrett, A. I., C. D. Westbrook, J. C. Nicol, and . H. M Stein, 2019: Rapid ice aggregation
813 process revealed through triple-wavelength Doppler spectrum radar analysis, *Atmos. Chem.*
814 *Phys.*, **19**, 5753–5769, doi:10.5194/acp-19-5753-2019

815 Bigg, E. K.: The supercooling of water, *Proc. Phys. Soc. B*, **66**, 688– 694, 1953.
816

817 Bodas-Salcedo, A., and Coauthors, 2011: COSP: Satellite simulation software for model
818 assessment. *Bull. Amer. Meteor. Soc.*, **92**, 1023–1043, doi: 10.1175/2011BAMS2856.1.

819 Boucher, O., and Coauthors, 2013: Clouds and aerosols. In *Climate Change 2013: The*
820 *Physical Science Basis. Contribution of Working Group I to the Fifth Assessment Report of*
821 *the Intergovernmental Panel on Climate Change* Stocker, T.F. and Coauthors, Eds.
822 Cambridge University Press, pp. 571-657, doi: 10.1017/CBO9781107415324.016.

823

824 Chepfer, H., S. Bony, D. Winker, G. Cesana, J. L. Dufresne, P. Minnis, C. J. Stubenrauch,
825 and S. Zeng, 2010: The GCM-Oriented CALIPSO Cloud Product (CALIPSO-GOCCP), *J.*
826 *Geophys. Res.*, **115**, D00H16, doi: 0.1029/2009JD012251

827

828 Connolly, P. J., C. Emersic, and P. R. Field, 2012: A laboratory investigation into the
829 aggregation efficiency of small ice crystals, *Atmos. Chem. Phys.*, **12**, 2055–2076,
830 https://doi.org/10.5194/acp-12-2055-2012.

831

832 Cotton, W.R. , G.J. Tripoli, R.M. Rauber, and E.A. Mulvihill, 1986: Numerical simulation of
833 the effects of varying ice crystal nucleation rates and aggregation processes on orographic
834 snowfall, *J. Climate Appl. Meteorol.*, **25**, 1658-1680, doi.org/10.1175/1520-
835 0450(1986)025<1658:NSOTEO>2.0.CO;2

836

837    Chellini, G., R. Gierens, and S. Kneifel, 2022: Ice aggregation in low-level mixed-phase
838    clouds at a high Arctic site: Enhanced by dendritic growth and absent close to the melting
839    level. *J. Geophys. Res.: Atmos.*, **127**, e2022JD036860. doi: 10.1029/2022JD036860

841    de Boer, G., Eloranta, E. W., & Shupe, M. D. (2009). Arctic mixed-phase stratiform cloud
842    properties from multiple years of surface-based measurements at two high-latitude locations.
843    *Journal of the Atmos. Sci.*, **66**(9), 2874–2887. https://doi.org/10.1175/2009JAS3029.

845    Dee D.P., and Coauthors, 2011: The ERA-Interim reanalysis: configuration and performance
846    of the data assimilation system, *Q.J.R. Meteorol. Soc*., **137**, 553-597, doi.org/10.1002/qj.828

848    Delanoë, J. ,and R. J. Hogan, 2010: Combined CloudSat-CALIPSO-MODIS retrievals of the
849    properties of ice clouds, *J. Geophys. Res.*, **115**, D00H29, doi: 10.1029/2009JD012346

851    Deshmukh, A., V. T. J. Phillips, A. Bansemer, S. Patade, and D. Waman, 2022: New
852    Empirical Formulation for the Sublimational Breakup of Graupel and Dendritic Snow, *J.*
853    *Atmos. Sci.*, **79**, 317–336, doi:10.1175/JAS-D-20-0275.1

855    Ebell, K., T. Nomokonova, M. Maturilli, and C. Ritter, 2020: Radiative Effect of Clouds at
856    Ny-Ålesund, Svalbard, as Inferred from Ground-Based Remote Sensing Observations, *J.*
857    *Appl. Meteor. Clim.*, **59**(1), 3-22, doi: 10.1175/JAMC-D-19-0080.1

859    Field., P., and Coauthors, 2017: Chapter 7: Secondary ice production - current state of the
860    science and recommendations for the future, Meteor. Monogr., **58**, 7.1–7.20 doi:
861    10.1002/2015GL065497

862    Gayet, J.-F., R. Treffeisen, A. Helbig, J. Bareiss, A. Matsuki, A. Herber, A. Schwarzenboeck,
863    2009: On the onset of the ice phase in boundary layer Arctic clouds, *J. Geophys. Res.*, **114**,
864    D19201, doi: 10.1029/2008jd011348

865    Georgakaki, P., G. Sotiropoulou, É. Vignon, A. C. Billault-Roux, A. Berne, and A. Nenes,
866    2022: Secondary ice production processes in wintertime alpine mixed-phase clouds, Atmos.
867    Chem. Phys., **22**, 1965–1988, doi: 10.5194/acp-22-1965-2022
868

869 Gettelman, A., and H. Morrison, 2015: Advanced Two-Moment Bulk Microphysics for

870 Global Models. Part I: Off-Line Tests and Comparison with Other Schemes, *J. Clim.*, **28**(3),

871 1268-1287, doi: 10.1175/JCLI-D-14-00102.1

872

873 Gossart, A., and Coauthors, 2017: Blowing snow detection from ground-based ceilometers:

874 application to East Antarctica, The Cryosphere, **11**, 2755–2772, https://doi.org/10.5194/tc-11-

875 2755-2017.

876

877 Hallett, J., and S. C. Mossop, 1974: Production of secondary ice particles during the riming

878 process, *Nature*, **249**, 26–28, doi: 10.1038/249026a0

879

880 Hogan, R. J., M. P. Mittermaier, and A. J. Illingworth, 2006: The Retrieval of Ice Water

881 Content from Radar Reflectivity Factor and Temperature and Its Use in Evaluating a

882 Mesoscale Model, *J. Appl. Meteor. Clim.*, **45**(2), 301-317, doi: 10.1175/JAM2340.1

883

884 Hoose, C., J. E. Kristjánsson, J.-P. Chen, and A. Hazra, 2010: A classical-theory-based

885 parameterization of heterogeneous ice nucleation by mineral dust, soot, and biological

886 particles in a global climate model. *J. Atmos. Sci.*, **67**(8), 2483–2503, doi:

887 10.1175/2010JAS3425.1

888

889 Hoose, C., and O. Möhler, 2012: Heterogeneous ice nucleation on atmospheric aerosols: a

890 review of results from laboratory experiments, *Atmos. Chem. Phys.*, **12**, 9817–9854, doi:

891 10.5194/acp-12-9817-2012

892

893 Illingworth, J., and Coauthors, 2007: Cloudnet, *Bull. Amer. Meteor. Soc.*, **88**(6), 883-898, doi:

894 10.1175/BAMS-88-6-883

895

896 Karlsson, L., R. Krejci, M. Koike, K. Ebell, and P. Zieger, 2021a: A long-term study of cloud

897 residuals from low-level Arctic clouds, Atmos. Chem. Phys., **21**, 8933–8959,

898 doi:10.5194/acp-21-8933-2021

899

900 Karlsson, L., R. Krejci, M. Koike, K. Ebell, and P. Zieger, 2021b: Arctic cloud and aerosol

901 measurements from Zeppelin Observatory, Svalbard, November 2015 to February 2018.

902 Dataset version 1. Bolin Centre Database. https://doi.org/10.17043/zeppelin-cloud-aerosol-1

903

904 Karrer, M., A. Seifert, D. Ori, and S. Kneifel, 2021: Improving the representation of

905 aggregation in a two-moment microphysical scheme with statistics of multi-frequency

906 Doppler radar observations, Atmos. Chem. Phys., **21**, 17133–17166, doi:10.5194/acp-21-

907 17133-2021

908

909 Kato, S., and Coauthors, 2018: Surface Irradiances of Edition 4.0 Clouds and the Earth's

910 Radiant Energy System (CERES) Energy Balanced and Filled (EBAF) Data Product, *Journal*

911 *of Climate*, **31**(11), 4501-4527, doi: 10.1175/JCLI-D-17-0523.1

912

913 Keinert, A., D. Spannagel, T. Leisner, and A. Kiselev, 2020: Secondary Ice Production upon

914 Freezing of Freely Falling Drizzle Droplets, *J. Atmos. Sci.*, **77**(8), 2959-2967, doi:

915 10.1175/JAS-D-20-0081.1

916

917 Kirkevåg, A., and Coauthors, 2018: A production-tagged aerosol module for Earth system

918 models, OsloAero5.3 – extensions and updates for CAM5.3-Oslo, Geosci. Model Dev., **11**,

919 3945–3982, doi:10.5194/gmd-11-3945-2018.

920

921 Kiszler, T., Ebell, K., and V Schemann, 2023: A performance baseline for the representation

922 of clouds and humidity in cloud-resolving ICON-LEM simulations in the Arctic. *Journal of*

923 *Advances in Modeling Earth Systems*, **15**, e2022MS003299. doi: 10.1029/2022MS003299

924

925 Korolev, A., and T. Leisner, 2020: Review of experimental studies of secondary ice

926 production, *Atmos. Chem. Phys.*, **20**, 11767–11797, doi: 10.5194/acp-20-11767-2020

927

928 Lauber, A., A. Kiselev, T. Pander, P. Handmann, and T. Leisner, 2018a: Secondary ice

929 formation during freezing of levitated droplets, *J. Atmos. Sci.*, **75**, 2815–2826, doi:

930 10.1175/JAS-D-18-0052.1

931

932 Lamb, D. and J. Verlinde, 2011: Physics and Chemistry of Clouds. Cambridge University

933 Press, Cambridge, doi: 10.1017/CBO9780511976377

934

935 Lawson, R. P, S. Woods, and H. Morrison., 2015: The microphysics of ice and precipitation

936 development in tropical cumulus clouds. *J. Atmos. Sci.*, **72**, 2429–2445, doi:/10.1175/JAS-D-

937 14-0274.1

938

939 Lloyd, G., and Coauthors, 2015: Observations and comparisons of cloud microphysical

940 properties in spring and summertime Arctic stratocumulus clouds during the ACCACIA

941 campaign, *Atmos. Chem. Phys.*, **15**, 3719–3737,  doi: 10.5194/acp-15-12953-2015

942

943 Löhnert, U., and S. Crewell, 2003: Accuracy of cloud liquid water path from ground-based

944 microwave radiometry 1. Dependency on cloud model statistics, *Radio Sci.*, 38, 8041,

945 doi:10.1029/2002RS002654

946

947 Luke, E.P., F. Yang, P.  Kollias, A.M.  Vogelmann, and M.,Maahn, 2021: New insights into

948 ice multiplication using remote-sensing observations of slightly supercooled mixed-phase

949 clouds in the Arctic. *Proceedings of the National Academy of Sciences,* **118**. doi:

950 10.1073/pnas.2021387118

951

952 Meyers, M. P., P. J. DeMott, and W.R. Cotton, 1992: New Primary Ice-Nucleation

953 Parameterizations in an Explicit Cloud Model. *Journal of Applied Meteorology (1988-

954 2005)*, **31**(7), 708–721, http://www.jstor.org/stable/26186583

955

956 Mizuno, H., 1990: Parameterization if the accretion process between different precipitation

957 elements. *J. Meteor. Soc. Japan*, **57**, 273-281, doi: 10.2151/jmsj1965.68.3_395

958

959 Morrison, H., J.A. Curry, V.I. Khvorostyanov, 2005: A New Double-Moment Microphysics

960 Parameterization for Application in Cloud and Climate Models. Part I: Description, *Atmos.

961 Sci., 62,* 3683-3704, doi: 10.1175/JAS3446.1

962

963 Morrison, H., G. De Boer, G. Feingold, J. Harrington, M.D. Shupe, and K. Sulia, 2012:

964 Resilience of persistent Arctic mixed-phase clouds, Nat. Geosci., **5**, 11–17, doi:

965 10.1038/ngeo1332

966 Murray, B. J., K. S. Carslaw, and P. R. Field, 2021: Opinion: cloud- phase climate feedback

and the importance of ice- nucleating particles, Atmos. Chem. Phys., **21**(2), 665– 679, doi: 10.5194/acp-21-665-2021

Naakka, T., T. Nygård, and T. Vihma, 2018: Arctic Humidity Inversions: Climatology and Processes. *J. Climate*, **31**, 3765–3787, doi: 10.1175/JCLI-D-17-0497.1

Nomokonova, T., K. Ebell, U,.Löhnert, M. Maturilli, C. Ritter, and E. O'Connor, 2019: Statistics on clouds and their relation to thermodynamic conditions at Ny-Ålesund using ground-based sensor synergy, Atmos. Chem. Phys., **19**, 4105–4126, https://doi.org/10.5194/acp-19-4105-2019.

Nomokonova, T., C. Ritter, and K. Ebell, 2019a: Liquid water path of HATPRO microwave radiometer at AWIPEV, Ny-Ålesund (2016). PANGAEA, doi: 10.1594/PANGAEA.902096

Nomokonova, T., C. Ritter, and K. Ebell, 2019b: Liquid water path of HATPRO microwave radiometer at AWIPEV, Ny-Ålesund (2017). PANGAEA, doi: 10.1594/PANGAEA.902098

Nomokonova, T., C. Ritter, and K. Ebell, 2019c: Liquid water path of HATPRO microwave radiometer at AWIPEV, Ny-Ålesund (2017). PANGAEA, doi: 10.1594/PANGAEA.902099

Nomokonova, T., and K. Ebell, 2019d: Cloud microphysical properties retrieved from ground-based remote sensing at Ny-Ålesund (10 June 2016 - 8 October 2018). University of Cologne, PANGAEA, doi: 10.1594/PANGAEA.898556

Nomokonova, T., C. Ritter, and K. Ebell, 2019e: Temperature profile of HATPRO microwave radiometer at AWIPEV, Ny-Ålesund (2016). PANGAEA, doi: 10.1594/PANGAEA.902145

Nomokonova, T., C. Ritter, and K. Ebell, 2019f: Temperature profile of HATPRO microwave radiometer at AWIPEV, Ny-Ålesund (2017). PANGAEA, doi: 10.1594/PANGAEA.902146

Nomokonova, T., C. Ritter, and K. Ebell, 2019g: Temperature profile of HATPRO microwave radiometer at AWIPEV, Ny-Ålesund (2018). PANGAEA, doi:

999    10.1594/PANGAEA.902147

1000

1001    Nomokonova, T., C. Ritter, and K. Ebell, 2019h: Integated water vapor of HATPRO
1002    microwave radiometer at AWIPEV, Ny-Ålesund (2016). PANGAEA, doi:
1003    10.1594/PANGAEA.902140

1004

1005    Nomokonova, T., C. Ritter, and K. Ebell, 2019i: Integated water vapor of HATPRO
1006    microwave radiometer at AWIPEV, Ny-Ålesund (2017). PANGAEA, doi:
1007    10.1594/PANGAEA.902142

1008

1009    Nomokonova, T., C. Ritter, and K. Ebell, 2019j: Integated water vapor of HATPRO
1010    microwave radiometer at AWIPEV, Ny-Ålesund (2018). PANGAEA, doi:
1011    10.1594/PANGAEA.902143

1012    Oraltay, R., and J. Hallett, 1989: Evaporation and melting of ice crystals: A laboratory
1013    study. *Atmos. Res.*, **24**, 169–189, doi:10.1016/0169-8095(89)90044-6

1014    Pasquier, J. T., and Coauthors, 2022: Conditions favorable for secondary ice production in
1015    Arctic mixed-phase clouds, Atmos. Chem. Phys. Discuss. [preprint],
1016    https://doi.org/10.5194/acp-2022-314

1017

1018    Passarelli, R. E., 1978: An Approximate Analytical Model of the Vapor Deposition and
1019    Aggregation Growth of Snowflakes, *J. Atmos. Sci.*, **35**(1), 118-124, doi: 0.1175/1520-
1020    0469(1978)035<0118:AAAMOT>2.0.CO;2

1021

1022    Phillips, V. T. J., M. Formenton, A. Bansemer, I. Kudzotsa, and B. Lienert, 2015). A
1023    Parameterization of Sticking Efficiency for Collisions of Snow and Graupel with Ice Crystals:
1024    Theory and Comparison with Observations, *J. Atmos. Sci.*, **72**(12), 4885-4902.

1025

1026    Phillips, V. T. J, J. I. Yano, A. Khain, 2017a: Ice multiplication by breakup in ice-ice
1027    collisions. Part I: Theoretical formulation, *J. Atmos. Sci.*, **74**, 1705 1719, doi: 10.1175/JAS-
1028    D-16-0224.1

1029

1030    Phillips, V. T. J., J. I. Yano, M. Formenton, E. Ilotoviz, V. Kanawade, I. Kudzotsa, J. Sun, A.

1031    Bansemer, A.G. Detwiler, A. Khain, and S.A., Tessendorf, 2017b: Ice multiplication by
1032    breakup in ice-ice collisions. Part II: Numerical simulations, J. Atmos. Sci., **74**, 2789–
1033    2811,doi: 10.1175/JAS-D-16-0223.1

1035    Phillips, V. T. J., S. Patade, J. Gutierrez, and A. Bansemer, 2018: Secondary Ice Production
1036    by Fragmentation of Freezing Drops: Formulation and Theory, *J. Atmos. Sci.*, **75**(9), 3031-
1037    3070, doi:10.1175/JAS-D-17-0190.1

1039    Rangno, A.L., and P.V. Hobbs, 2001: Ice particles in stratiform clouds in the Arctic and
1040    possible mechanisms for the production of high ice concentrations, *J. Geophys. Res.*, **106**,
1041    15065–15075, doi: 10.5194/acp-19-5293-2019

1043    Reisner, J., R. M. Rasmussen, and R. T. Bruintjes, 1998: Explicit forecasting of supercooled
1044    liquid water in winter storms using the MM5 mesoscale model, *Quart. J. Roy. Meteor. Soc.*,
1045    **124**(548), 1071-1107, doi: 10.1002/qj.49712454804

1047    Schmeisser, L., and Coauthors, 2018: Seasonality of aerosol optical properties in the Arctic,
1048    Atmos. Chem. Phys., 18, 11599–11622, https://doi.org/10.5194/acp-18-11599-2018.

1050    Schwarzenboeck, A., V. Shcherbakov, R. Lefevre, J. F. Gayet, Y. Pointin, and C. Duroure,
1051    2009: Indications for stellar-crystal fragmentation in Arctic clouds, Atmos. Res., **92,** 220–
1052    228, doi: 10.1016/j.atmosres.2008.10.002

1053    Seinfeld J. H., and Coauthors, 2016: Improving our fundamental understanding of the role of
1054    aerosol-cloud interactions in the climate system. *Proc. Natl. Acad. Sci. USA*, **113**(21), 5781–
1055    5790, doi:10.1073/pnas.1514043113

1057    Seland, Ø., and Coauthors, 2020: Overview of the Norwegian Earth System Model
1058    (NorESM2) and key climate response of CMIP6 DECK, historical, and scenario simulations,
1059    *Geosci. Model Dev.*, **13**, 6165–6200, doi: 10.5194/gmd-13-6165-2020

1061    Shaw, J., Z. McGraw, O. Bruno, T. Storelvmo, and S. Hofer, 2022: Using satellite
1062    observations to evaluate model microphysical representation of Arctic mixed-phase

clouds. *Geophysical Research Letters*, **49**, e2021GL096191. doi: 10.1029/2021GL096191

Shupe, M. D, S. Y. Matrosov, and T. Uttal, 2006: Arctic Mixed-Phase Cloud Properties Derived from Surface-Based Sensors at SHEBA, *J. Atmos. Sci.*, **63**(2), 697-711, doi: 10.1175/JAS3659.1

Shupe, M. D., V. P. Walden, E. Eloranta, T. Uttal, J. R. Campbell, S. M. Starkweather, and M. Shiobara, 2011: Clouds at Arctic at- mospheric observatories. Part I: Occurrence and macro- physical properties. J. Appl. Meteor. Climatol., **50**, 626–644, doi:10.1175/2010JAMC2467.1.

Sledd, A., and T. L'Ecuyer, 2021: Uncertainty in Forced and Natural Arctic Solar Absorption Variations in CMIP6 Models, *Journal of Climate*, **34**(3), 931-948. 10.1175/JCLI-D-20-0244.1

Storelvmo, T., 2017: Aerosol Effects on Climate via Mixed-Phase and Ice Clouds. *Annual Review of Earth and Planetary Sciences,* **45**, 199-222, doi:10.1146/ANNUREV-EARTH-060115-012240

Sotiropoulou, G., S. Sullivan, J. Savre, G. Lloyd, T. Lachlan-Cope, A. M. L. Ekman, and A. Nenes, 2020: The impact of secondary ice production on Arctic stratocumulus, Atmos. Chem. Phys., **20**, 1301–1316, doi: 10.5194/acp-20-1301-2020

Sotiropoulou, G., É. Vignon, G. Young, H. Morrison, S. J. O'Shea, T. Lachlan-Cope, A. Berne, and A. Nenes, 2021a: Secondary ice production in summer clouds over the Antarctic coast: an underappreciated process in atmospheric models, Atmos. Chem. Phys., **21**, 755–771, doi: 10.5194/acp-21-755-2021

Sotiropoulou, G., L. Ickes, A. Nenes, A., and A.M.L. Ekman, 2021b: Ice multiplication from ice–ice collisions in the high Arctic: sensitivity to ice habit, rimed fraction, ice type and uncertainties in the numerical description of the process, Atmos. Chem. Phys., **21**, 9741–9760, doi: 10.5194/acp-21-9741-2021.

Sullivan, S. C., A. Kiselev, T. Leisner, C. Hoose, ans A. Nenes, 2018: Initiation of secondary ice production in clouds, *Atmos. Chem. Phys.*, **18**, 1593–1610, doi: 10.5194/acp-18-1593-2018

1096

1097 Takahashi, T., Y. Nagao, and Y. Kushiyama, 1995: Possible high ice particle production

1098 during graupel-graupel collisions, *J. Atmos. Sci.*, **52**, 4523–4527

1099

1100 Tan, I., and T. Storelvmo, 2019: Evidence of strong contributions from mixed-phase clouds to

1101 Arctic climate change. *Geophys. Res. Let.,* **46**, 2894– 2902, doi: 10.1029/2018GL081871

1102

1103 Tjernström, M., and Coauthors, 2012: Meteorological conditions in the central Arctic summer

1104 during the Arctic Summer Cloud Ocean Study (ASCOS), *Atmos. Chem. Phys.*, **12**, 6863–

1105 6889, doi: 10.5194/acp-12-6863-2012

1106

1107 Thomas, M. A., A. Devasthale, T. L'Ecuyer, S. Wang, T. Koenigk and K. Wyser, 2019:

1108 Snowfall distribution and its response to the Arctic Oscillation: an evaluation of HighResMIP

1109 models in the Arctic using CPR/CloudSat observations, *Geosci. Model Dev.*, **12**, 3759–3772,

1110 doi:10.5194/gmd-12-3759-2019

1111

1112 Vardiman, L., 1978: The generation of secondary ice particles in clouds by crystal-crystal

1113 collision, J. *Atmos. Sci.*, **35**, 2168–2180, doi: 0.1175/1520-

1114 0469(1978)035<2168:TGOSIP>2.0.CO;2,

1115

1116 Vignesh, P. P., J. H. Jiang, P. Kishore, H. Su, T. Smay, N. Brighton, and I. Velicogna, 2020:

1117 Assessment ofCMIP6 cloud fraction and comparisonwith satellite observations.Earth and

1118 Space Science, **7**, e2019EA000975.  doi: 10.1029/2019EA000975

1119

1120 Wang, Y., X. Liu, C. Hoose, C., and B. Wang, 2014: Different contact angle distributions for

1121 heterogeneous ice nucleation in the Community Atmospheric Model version 5. *Atmos. Chem.*

1122 *Phys.*, **14**(19), 10411–10430, doi: 10.5194/acp-14-10411-2014

1123

1124 Wex, H., and Coauthors, 2019: Annual variability of ice-nucleating particle concentrations at

1125 different Arctic locations, *Atmos. Chem. Phys.*, **19**, 5293-5311, doi:10.5194/acp-19-5293-

1126 2019

1127

1128 Wielicki, B. A., B. R. Barkstrom, E. F. Harrison, R. B. III Lee, G. L.  Smith, and J. E. Cooper,

1129  1996:  Clouds and the Earth's Radiant Energy System (CERES): An Earth Observing System

1130  Experiment, *Bull. Amer. Meteorol. Soc.*, **77**(5), 853-868, doi: ulletin of the American

1131  Meteorological           Society,           **77**(5),           853-868,           doi: 10.1175/1520-

1132  0477(1996)077<0853:CATERE>2.0.CO;2.

1133

1134  Wyszyński  P.and R.Przybylak, 2014: Variability of humidity conditions in the Arctic during
1135  the    first    International    Polar    Year,    1882–83,    *Polar    Research*,    33:1,    doi:
1136  10.3402/polar.v33.23896
1137

1138  Young, K. C., 1974: The Role of Contact Nucleation in Ice Phase Initiation in Clouds,

1139  *Journal of Atmospheric Sciences*, **31**(3), 768-776.

1140

1141  Zelinka, M. D., and Coauthors, 2020: Causes of higher climate sensitivity in CMIP6 models.

1142  Geophys. Res. Lett., **47**, e2019GL085782, doi:10.1029/2019GL085782.

1143

1144  Zhao, X., X. Liu, V. T. J. Phillips, and S. Patade, 2021: Impacts of secondary ice production

1145  on Arctic mixed-phase clouds based on ARM observations and CAM6 single-column model

1146  simulations, *Atmos. Chem. Phys.*, **21**, 5685–5703, doi: 10.1029/2021GL092581

1147

1148  Zhao, X., and X. Liu, 2021: Global importance of secondary ice production. *Geophys. Res.*

1149  *Let.*, **48**, e2021GL092581, doi: 10.1029/2021GL092581

1150

1151  Zhao, X., and X. Liu, 2022: Relative importance and interactions of primary and secondary

1152  ice production in the Arctic mixed-phase clouds*, Atmos. Chem. Phys.*, **22**, 2585–2600,

1153  doi: 10.5194/acp-2021-686

1154